JOURNAL OF MATERIALS RESEARCH AND TECHNOLOGY 2023;26:6703–6718

Available online at www.sciencedirect.com

jmr&t Journal of Materials Research and Technology

journal homepage: www.elsevier.com/locate/jmrt

Effect of austempering temperature on microstructure evolution, mechanical properties and wear resistance of carbon-free nano-bainite steel

Enmao Wang [a], *Qianxi He* [b], *Chen Gu* [c], *Yong Wang* [d], *Haoxiu Chen* [e], *Yingjian Che* [a], *R.D.K. Misra* [f], *Na Gong* [g], *Huibin Wu* [a,**], *Gang Niu* [a,*]

[a] *Collaborative Innovation Center of Steel Technology, University of Science and Technology Beijing, Beijing, 100083, China*

[b] *McMaster Manufacturing Research Institute (MMRI), McMaster University, Hamilton, ON, L8P 0A6, Canada*

[c] *Department of Materials Science and Engineering, McMaster University, Hamilton, ON, L8S 4L7, Canada*

[d] *School of Materials Science and Engineering, Nanyang Technological University, Singapore, 639798, Singapore*

[e] *Department of Materials Science and Engineering, University of Toronto, Toronto, ON, M5S 3E4, Canada*

[f] *Laboratory for Excellence in Advanced Steel Research, Department of Metallurgical, Materials and Biomedical Engineering, University of Texas at El Paso, El Paso, TX 79968, USA*

[g] *Institute of Materials Research and Engineering, Agency for Science, Technology and Research, Singapore 138634, Singapore*

ARTICLE INFO

Article history:
Received 4 July 2023
Accepted 6 September 2023
Available online 12 September 2023

Keywords:
Nano-bainite
Austempering
Microstructure
Mechanical property
Wear resistance
Retained austenite

ABSTRACT

Carbide-free nano-bainite steel holds significant potential for applications in mining as an ultra-high strength wear-resistant steel, but the wear mechanisms are not yet fully understood. This study aims to explore the effect of austempering temperature on microstructure, mechanical properties and wear resistance of carbide-free nano-bainitic steel. The relationship between the content and mechanical stability of retained austenite (RA) and mechanical properties was investigated to elucidate the mechanisms of pin-on-disc wear and impact wear. The results show that in the range of M_S~300 °C, the phase transformation incubation period and completion time significantly increase with decreasing austempering temperature, which is mainly related to higher phase transformation driving force resulting from a larger subcooling degree and slow growth of carbon content in RA. Optimal strength and hardness of 2099 MPa and 615 HBW, respectively, are achieved after austempering at 210 °C for 83 h. Austempering at 270 °C for 11 h yields the best balance of strength and plasticity, with a strength-plasticity product of 28.8 GPa%. The micro-cutting mechanism of pin-on-disc wear leads to serious weight loss. The RA with poor mechanical stability accelerates the stress-induced martensite transformation, while internal stress support due to volume expansion reduces the penetration depth of abrasive particles. The weight loss in impact wear is primarily caused by shedding due to fatigue failure. With the increase of RA content and mechanical stability, the

* Corresponding author.
** Corresponding author.
E-mail addresses: whbustb@163.com (H. Wu), ustbniug@163.com (G. Niu).

https://doi.org/10.1016/j.jmrt.2023.09.059

persistent stress-induced martensite transformation effectively hinders micro-crack propagation, thereby enhancing impact wear resistance.

1. Introduction

The global mining industry faces several challenges, including the depletion of high-grade ore, complex mining conditions, and deep-well operations. To address these challenges, open-pit mining technology is evolving towards continuous production and the use of large-scale equipment [1,2]. A fundamental requirement for mining components is excellent wear resistance. The wear resistance of steel is affected by various factors, including microstructure type and mechanical properties, which can vary under different wear conditions [3]. Nowadays, most low-alloy high-strength wear-resistant steels are martensite steels, characterized by limited plasticity-toughness and low resistance to delayed fracture, significantly impacting service life and safety [4]. In enhance the wear resistance of materials, the scholars and teams have proposed various methods, such as alloying, surface treatment and structural modification through heat treatment adjustments [5,6]. Thus, there is a need for the development of novel wear-resistant steels to overcome these limitations.

Carbide-free nano-bainite steel was originally designed as a novel structural steel for armor and bearings [7–9]. By incorporating approximately 1.5 wt% silicon, the precipitation of brittle cementite can be effectively suppressed, allowing for enhanced the carbon enrichment in metastable RA. As a result, this steel exhibits a fine microstructure and achieves excellent comprehensive properties [10,11]. The remarkable combination of high strength and high hardness arises from the presence of nanoscale ultrafine laths and dislocation strengthening, while the high plasticity stems from strain-induced martensite transformation during deformation or the formation of twins in RA [12]. Behadeshia et al. [13] illustrated the benefit of RA in achieving additional strain hardening, as the energy required for austenite to martensite transformation during deformation contributes to the mechanical properties even after tempering. Zhang et al. [14] explored the microstructure evolution during bainite transformation and tensile deformation during austempering in-depth, revealing various lengths of nano-bainite laths and RA with diverse sizes and shapes. They achieved a tensile strength (TS) of ~1550 MPa, a uniform elongation of ~30% and an impact toughness of ~80 J in a high-C high-Si bainite steel. Xu et al. [15] investigated the effect of austempering process on the mechanical properties of nano-bainite steels by performing one-step and two-step austempering above and below the M_s point, respectively. Although the tensile strength was around 1100 MPa, the total elongation (TE) reached 18.2%. Lee et al. [16] explored the effect of austempering temperature on the microstructure and mechanical properties of high-carbon nano-bainite steels. They demonstrated that the volume fraction of bainite ferrite (BF), blocky and film-like RA could be controlled by adjusting the austempering temperature, highlighting the significance of mechanical stability in developing nano-bainite steels.

In recent years, the exceptional mechanical properties of carbide-free nano-bainite steels have prompted their exploration in the field of wear resistance, gaining recognition among researchers. Qin et al. [17] revealed that high carbon nano-bainite bearing steels, characterized by equivalent initial hardness and absence of carbide precipitation, developed a protective non-destructive oxide layer upon the sliding wear surface. Combined with RA, it exhibited remarkable resistance to sliding wear. Recent studies have shown that the wear resistance of nano-bainite steels outperforms tempered martensite steels and other bainite steels [18–20]. This is due to the more refined microstructure, which not only provides high strength, but also effectively impedes the propagation of cracks during wear, allowing the material to withstand severe plastic deformation and impact [21]. Regarding the role of austenite in the wear process, it has been found that a certain amount of RA in the matrix contributes to reduced weight loss. However, the morphology of austenite also has different effects on wear behavior. Blocky austenite generally exhibits lower mechanical stability compared to film-like austenite, and tends to transform preferentially into hard martensite during plastic deformation, thus becoming a potential source of crack initiation [22]. On the other hand, film-like austenite has been observed to inhibit the initiation of fatigue cracks, mainly due to the mechanism of transformation induced crack termination (TICT) [23]. Obviously, the outstanding performance of carbide-free nano-bainite steel in the wear process can be attributed not only to the benefit of ultra-fine BF laths but also to the interphase distribution of film-like RA. However, current research on the wear resistance of carbide-free nano-bainite steel is predominantly limited to a single wear behavior, with a particular gap in understanding the impact wear mechanism and the role of RA in wear, necessitating more comprehensive and systematic investigations.

In this study, the effect of austempering temperature above M_s point on the microstructure, mechanical properties, and wear resistance of carbide-free nano-bainite steels has been explored with the aim of low cost and enhanced wear resistance. Additionally, the relationship between the content and mechanical stability of RA and mechanical properties has been established. Subsequently, the wear characteristics and mechanisms of carbide-free nano-bainite steels have been analyzed by pin-on-disc wear and impact wear, which provide a theoretical foundation for their extensive application in the field of wear.

2. Materials and methods

2.1. Materials and process

The composition of the studied steel under investigation is carefully designed to achieve a balance between low cost and exceptional wear resistance. High C content is advantageous

Table 1 – Dominant chemical composition of the studied steel (wt.%).

Elements	C	Si	Mn	Cr	Al	S	P	Fe
wt.%	0.88	2.46	1.14	1.03	0.93	0.007	0.0078	Bal.

in widening the temperature difference between B_s and M_s [24]. The content of Cr and Mn should be increased to broaden the bainite transformation zone. To ensure that carbide-free bainite is obtained, sufficient amounts of Si and Al are added, with the Si content controlled below 2.5 wt% to prevent casting-related cracking [25,26]. In addition, the presence of Al accelerates the bainite transformation, leading to a shorter production cycle. The dominant chemical composition of the studied steel is shown in Table 1.

The heat treatment process of the studied steel is illustrated in Fig. 1. Initially, the studied steel was smelted using a vacuum medium frequency induction melting furnace and cast into ingot. After holding the ingot at 1100 °C for 1 h, the ingot was hot forged into round bar of Φ32 mm at no less than 900 °C and subsequently furnace cooled to room temperature. The microstructure of the studied steel after forging was lamellar pearlite. A standard specimen of Φ4 mm × 10 mm was cut from the forged ingot, and the phase transformation temperature of the steel was measured by the expansion method (A_{ccm} = 849 °C, A_{c1} = 743 °C). The B_S and M_S were calculated by the MUCG83 software to be 348 °C and 183 °C, respectively. In eliminate the lamellar pearlite in the forged steel and improve the quenching property, spheroidizing annealing treatment was adopted to obtain the granular pearlite: holding in a chamber furnace at 800 °C for 2 h, then furnace cooling to 720 °C, and holding for 6 h before being removed for air cooling. Samples of Φ4 mm × 10 mm were cut from ingots to investigate the austempering transformation kinetics. Following complete austenitization at 1000 °C for 15 min, the samples were cooled to 270 °C, 240 °C and 210 °C at a rate of 10 °C/s, respectively, and then cooled to room temperature after completing the phase transformation. The austempering experiments were carried out in a double hearth salt bath furnace using the final treatment process as shown in Fig. 1 with the sample size of Φ32 mm × 70 mm.

2.2. Mechanical tests

The tensile samples were made of standard round bars with a gauge length of 25 mm as specified in ASTM E8, and the tensile tests were carried out on a CMT5105 microcomputer-controlled electronic universal tensile tester at a rate of 1.5 mm/min. The surface Brinell hardness of the samples was tested using a Brinell hardness tester model HBS-3000. All mechanical tests were conducted multiple times to obtain average value.

2.3. Wear tests

The pin-on-disc wear test was performed by sliding the sample's surface to be worn on the abrasive paper at a specified speed under a load, and the schematic diagram of the test setup is shown in Fig. 2(a), and the microstructure of the abrasive paper used is shown in Fig. 2(b). The wear resistance of the samples was determined by measuring the weight loss of the samples before and after wear. The sample size was Φ4 mm × 10 mm, and a pre-wear test (F_N = 7 N, 2000 mesh abrasive paper) was performed for 200 r before the formal test. Following the pre-wear test, the sample was ultrasonically cleaned with acetone and blown dry. The weight of the sample was weighed on an analytical balance with an accuracy of 1 mg and recorded as W_0. The formal wear test (F_N = 7 N, 200 mesh abrasive paper) was performed at a constant speed of 70 r/min for 200 r. The worn samples were weighed as W_1 after cleaning and blowing dry. The samples were tested three times for each process and the weight loss ΔW ($\Delta W = W_0 - W_1$) was averaged.

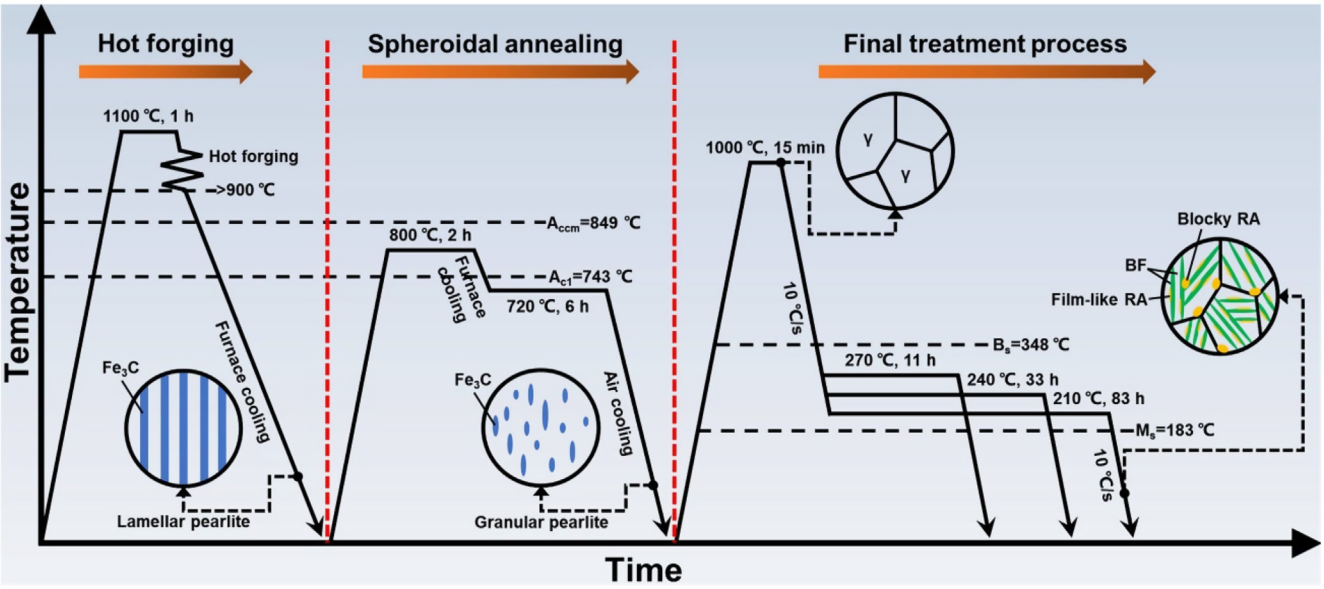

Fig. 1 – Heat treatment process of the studied steel.

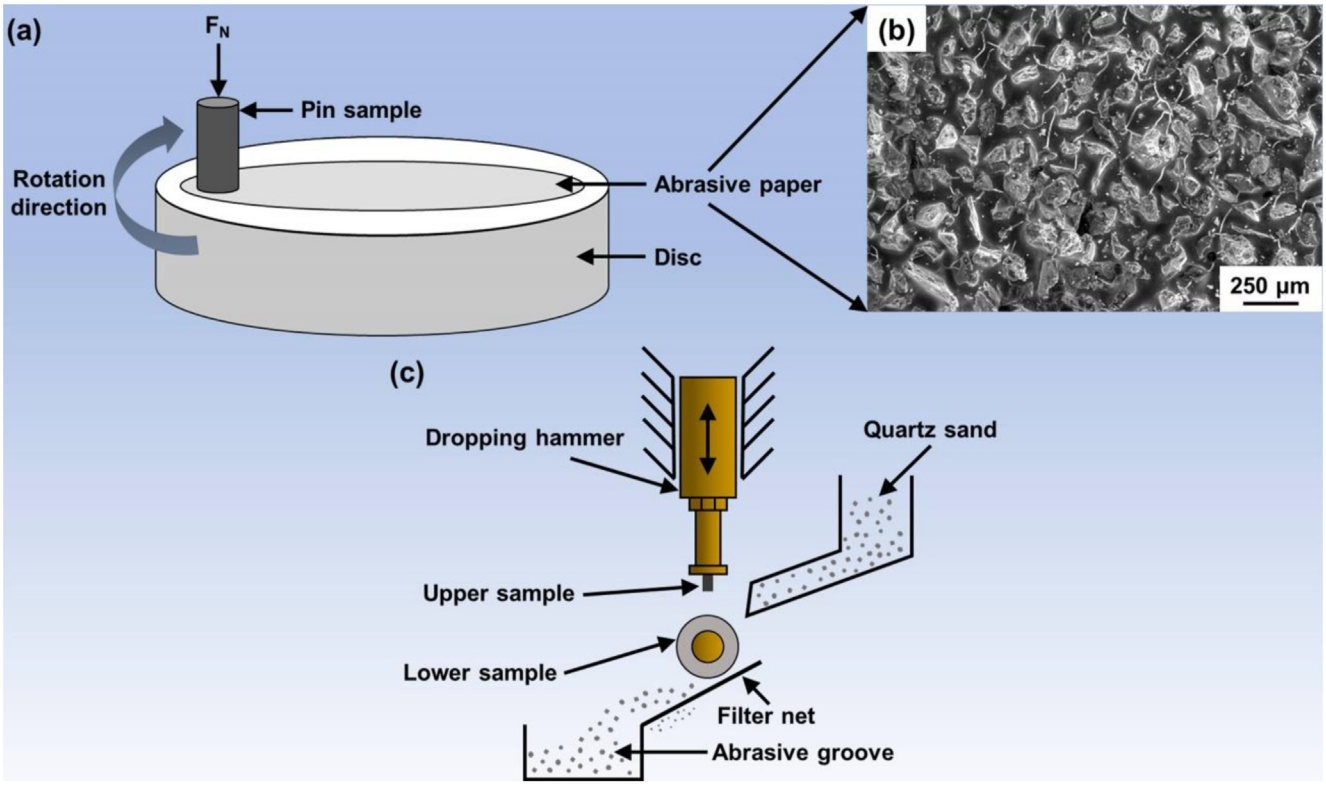

Fig. 2 – (a) Schematic diagram of pin-on-disc wear; (b) SEM image of abrasive paper; (c) schematic diagram of impact wear.

The schematic diagram of impact wear is shown in Fig. 2(c). Wear resistance was measured by friction of the studied steel (upper sample) and bearing steel (lower sample) with dry abrasive (quartz sand) under impact load. The dimension of the upper sample was 10 mm × 10 mm × 30 mm, and the impact energy was 5 J. The samples were unloaded for 30 min prior to the formal test. The samples were weighed before and after 0.5 h, 1 h and 1.5 h of the formal test. The weight loss was calculated in the same way as pin-on-disc wear.

2.4. *Microstructure characterization*

The metallographic samples were cut from the heat-treated steel, polished on sandpaper with different particle sizes in turn, and eroded with 4 vol% nitric acid alcohol solution after mechanical polishing. The microstructure morphology was observed on an optical microscope (OM, AX-10) and field emission scanning electron microscope (SEM, ZEISS ULTRA 55), respectively. The surface morphology and wear scar depth of the steel after pin-on-disc wear were observed using SEM and confocal laser scanning microscopy (CLSM, LEXT OLS4100). The 3D morphology of the worn surface was reconstructed by LEXT OLS4100 software. The samples after impact wear were cut along the midline, and the morphology was observed by SEM after polishing and erosion. The phase composition and austenite content of the studied steels were analyzed using an X-ray diffractometer (XRD, D/MAX-RB) (CuKα, voltage 40 kV, current 150 mA, step size 0.02°, scanning speed 1°/min). The size of XRD sample was 10 mm × 15 mm. After mechanical grinding, the samples were electropolished in solution (10 vol% glycerol + 20 vol% perchloric acid + 70 vol% alcohol). The diffraction peaks of carbides were not observed by XRD. The integrated intensities of (200)γ, (220)γ and (311)γ peaks of austenite, and the (200)α and (211)α peaks of ferrite were calculated by Jade 6.5, respectively. The volume fraction of RA (V_{RA}) was quantified via the following equation [27]:

$$V_{RA} = \frac{\frac{1}{n}\sum_{j=1}^{n}\frac{I_\gamma^j}{R_\gamma^j}}{\frac{1}{n}\sum_{j=1}^{n}\frac{I_\gamma^j}{R_\gamma^j}+\frac{1}{n}\sum_{j=1}^{n}\frac{I_\alpha^j}{R_\alpha^j}} \quad (1)$$

where n is the number of detected diffraction peaks, I is the integrated intensity of the diffraction peak, R is the material scattering factor ($R = (1/V^2)F^2P((1+\cos^2 2\theta)/\sin\theta\sin 2\theta)e^{-2m}$), V is the volume of unit cell, F is the structure factor, P is the multiplicity factor, e^{-2m} is the temperature factor, and $(1+\cos^2 2\theta)/\sin\theta\sin 2\theta$ is the angle factor. The lattice constant (a_γ) of RA was calculated by bringing the diffraction peak information into the equation, and the carbon content (C_γ) in RA was calculated with the assistance of the Dyson-Holmes equation [28] :

$$a_\gamma = 3.578 + 0.033C_\gamma \quad (2a)$$

$$C_\gamma = \left(\frac{\lambda\sqrt{h^2+k^2+l^2}}{2\sin\theta} - 3.578\right) \Big/ 0.033 \quad (3)$$

The fine lath microstructure was observed by transmission electron microscopy (TEM, FEI F20). The TEM samples were ground to 50 μm and then diluted by the double-jet polishing

technique (5 vol% perchloric acid solution + 95 vol% absolute ethanol).

3. Results

3.1. *Effect of austempering temperature on microstructure evolution*

Fig. 3(a) presents the austempering dilatometric curves of the studied steel at different temperatures. At the initial stage of austempering, there is a short phase transformation incubation period in the dilatometric curves. Typically, the time required to achieve 3 vol% bainite is considered as the phase transformation incubation period, while the time needed to reach 98 vol% bainite is regarded as an indication of the completion of phase transformation [29]. During the austempering process, the amount of austenite transformation is positively correlated with the amount of expansion. Therefore, the lever method can be employed to calculate the extent of bainite phase transformation, as depicted in Fig. 3(b).

As the austempering temperature decreases, the phase transformation incubation period continues to extend, which is about 0.7 h, 1.9 h and 3.6 h at 270 °C, 240 °C, and 210 °C, respectively. Fig. 3(c) illustrates a decrease in the maximum phase transformation rate and a delay in its appearance time. Continuing to austempering, the phase transformation causes volume expansion, and the phase transformation rate increases before eventually decreasing. After a certain period, the expansion curve remains parallel, indicating the completion of the phase transformation. With the decrease of austempering temperature, the time required to complete the phase transformation is prolonged, specifically 7.8 h and 28.4 h at 270 °C and 240 °C, respectively. Due to the limitation of austempering time in the dilatometer, the austempering time at 210 °C is set to 60 h. It can be seen from the figure that the expansion of the studied steel tends to be gentle after austempering for 60 h but does not reach its maximum value,

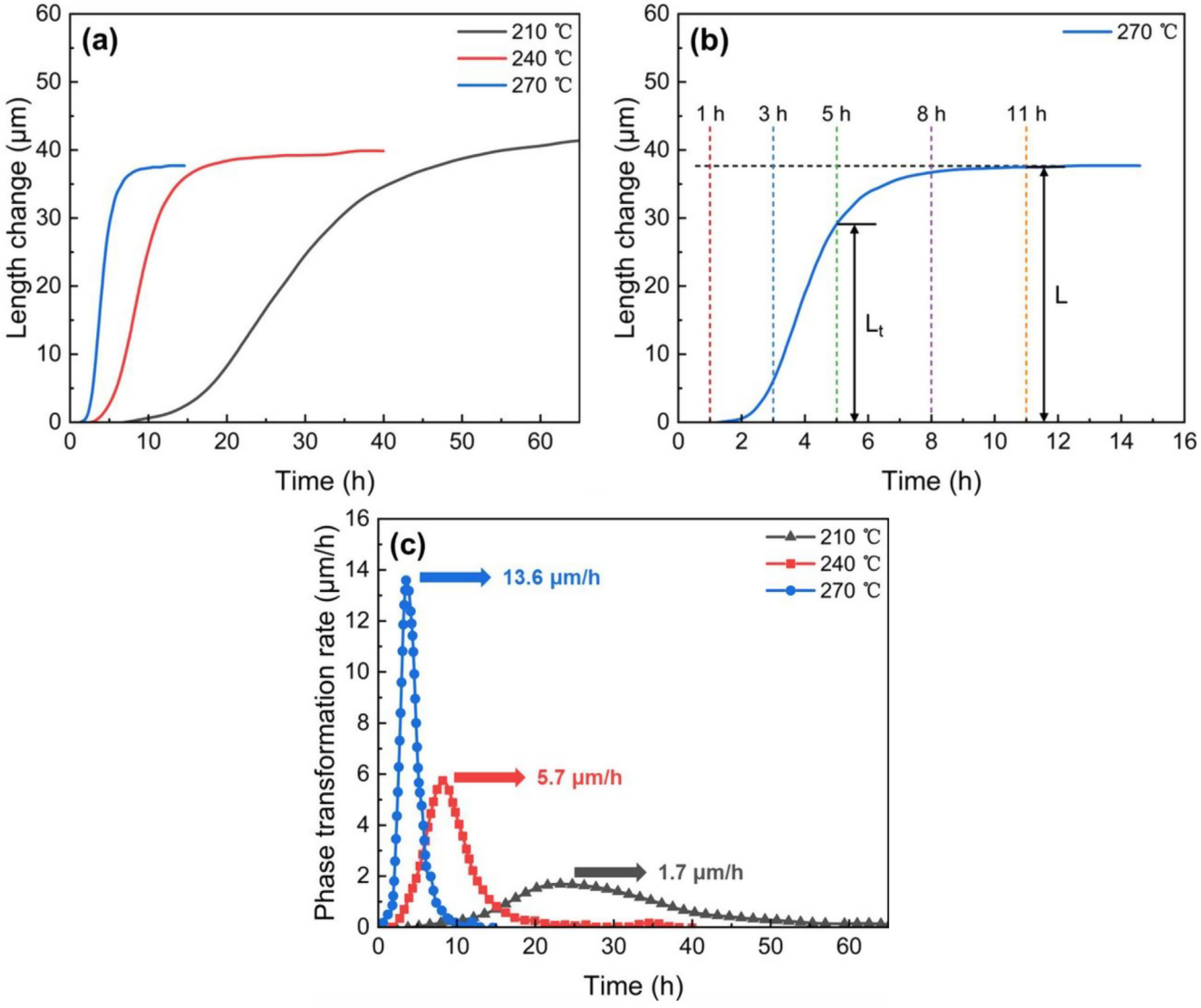

Fig. 3 – (a) Dilatometric curves; (b) calculation of bainite transformation degree by lever method; (c) bainite phase transformation rate of the studied steel during austempering at different temperatures.

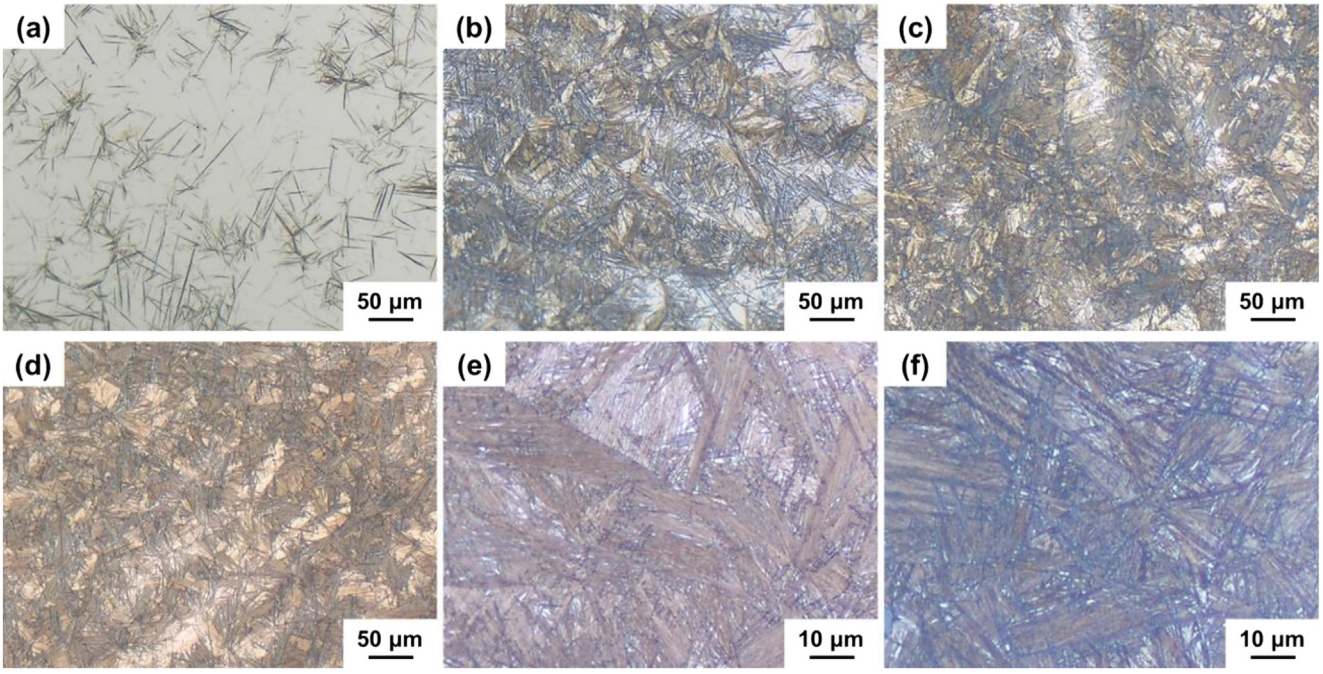

Fig. 4 – Optical micrographs of the studied steel after austempering at 210 °C for different times: (a) 11 h; (b) 23 h; (c) 35 h; (d) 60 h; (e) 72 h; (f) 83 h.

demonstrating the phase transformation has not yet been completed. Combined with the metallographic results, it is determined that the completion time of phase transformation at 210 °C is approximately 80 h. The observed phenomenon is mainly attributed to the diffusion coefficient of C atoms (other substitutional atoms do not partition in austenite and bainite ferrite) and the supercooled austenite [30]. At the initial stage of bainite transformation, the carbon-depleted zone and carbon-enriched zone need to be divided by the diffusion of C atoms [31]. The decrease in diffusion coefficient prolongs the time of forming a carbon-depleted zone, which leads to a significant increase in the bainite transformation incubation period. Although the increase of austenite undercooling enhances the driving force of phase transformation, the lower austempering temperature leads to the decreased diffusion rate of C atoms from bainite ferrite to austenite.

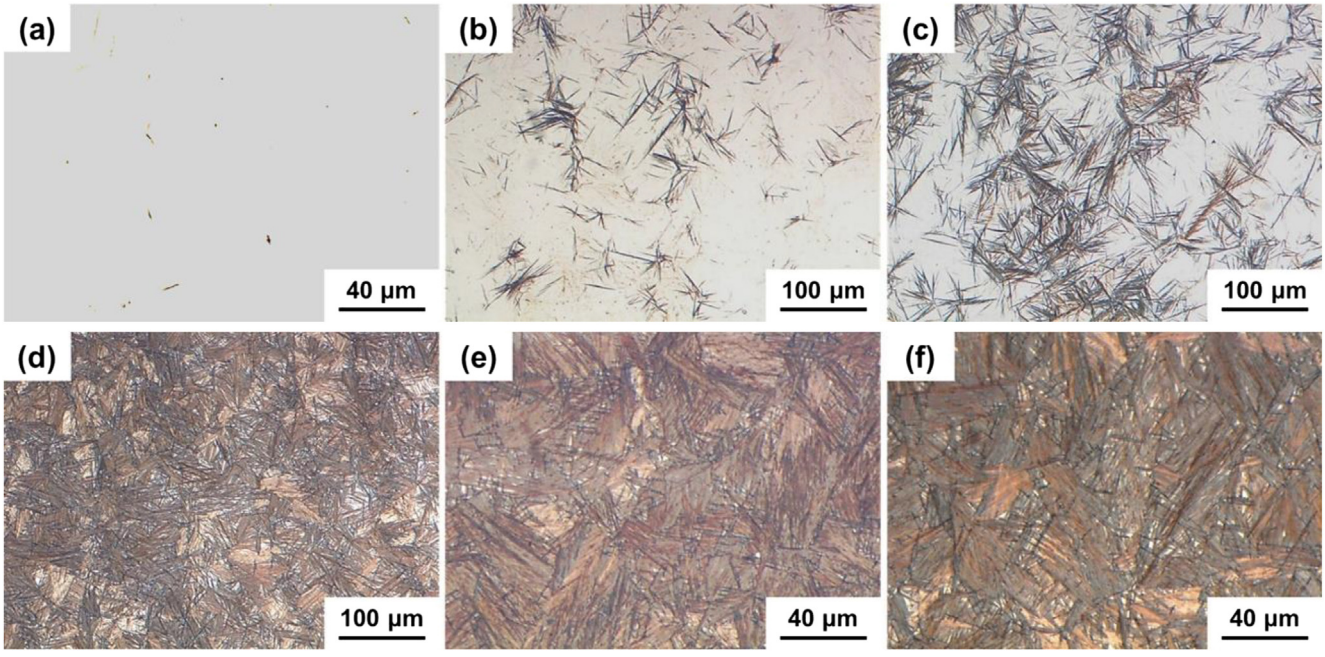

Fig. 5 – Optical micrographs of the studied steel after austempering at 240 °C for different times: (a) 1 h; (b) 3 h; (c) 5 h; (d) 10 h; (e) 22 h; (f) 33 h.

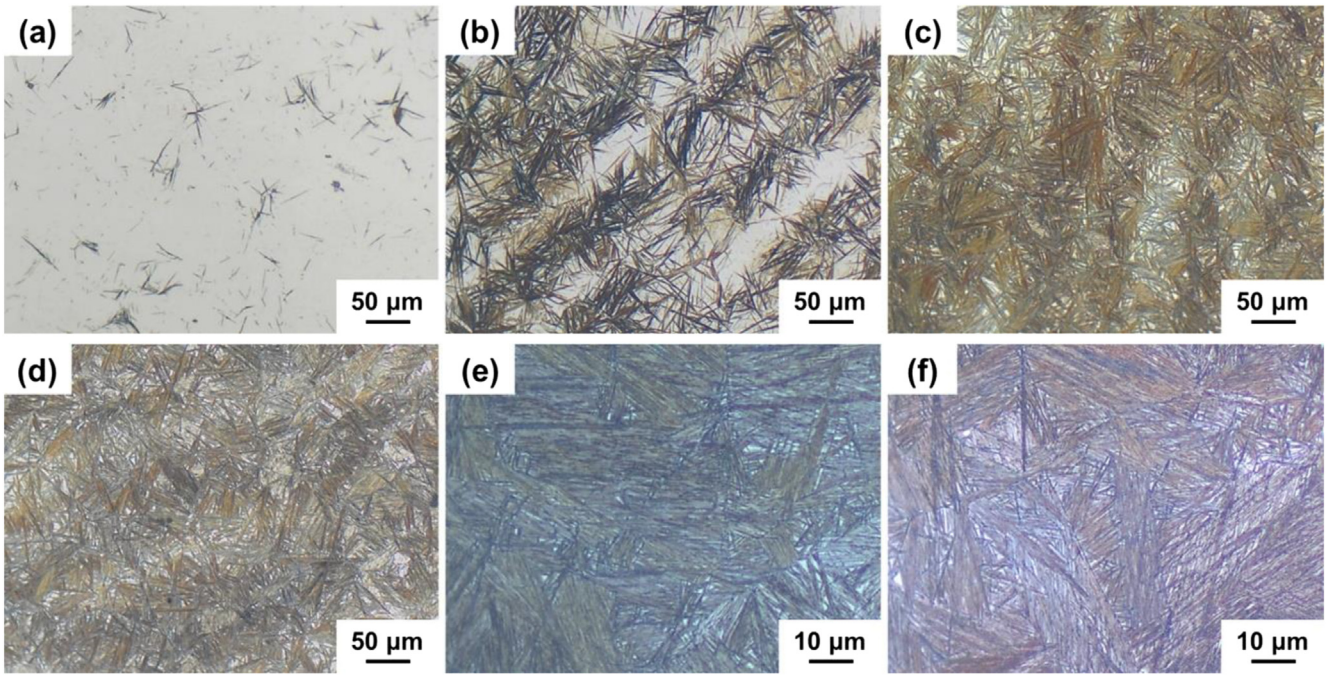

Fig. 6 – Optical micrographs of the studied steel after austempering at 270 °C for different times: (a) 1 h; (b) 3 h; (c) 5 h; (d) 7 h; (e) 9 h; (f) 11 h.

Fig. 4 shows the optical micrographs of the studied steel austempering at 210 °C. The bainite phase transformation occurs after 11 h and a small amount of gray acicular structure begins to appear. The acicular bainite increases significantly from 23 h. As the bainite phase transformation progresses until 83 h, the presence of almost full acicular structure implies the completion of the bainite phase transformation at this time. Fig. 5 shows the optical micrographs at 240 °C. The acicular bainite does not appear after austempering for 1 h, indicating that it is still in the phase transformation incubation period. However, the appearance of a small amount of acicular bainite after 3 h shows the initiation of the phase transformation, which then fully completes after 33 h. With the increasing of austempering temperature to 270 °C, the phase transformation begins at 1 h and completes at 11 h, as shown in Fig. 6. Compared with austempering at 210 °C, both the bainite phase transformation incubation period and the time required for the completion of phase transformation have significantly shortened, which aligns well with the results of the dilatometric curves.

The variations in RA content of the studied steel during austempering at different temperatures are shown in Fig. 7. When austempering at the beginning, there is either no bainite phase transformation or only a small amount occurs. During

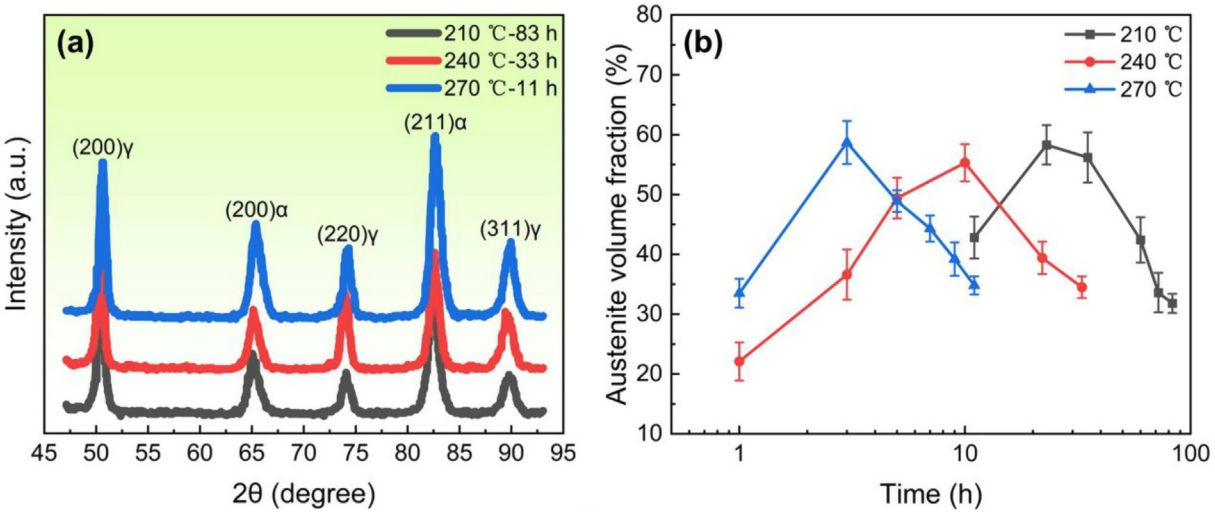

Fig. 7 – (a) XRD patterns of the studied steel at different processes; (b) changes of austenite volume fraction over time at different austempering temperatures.

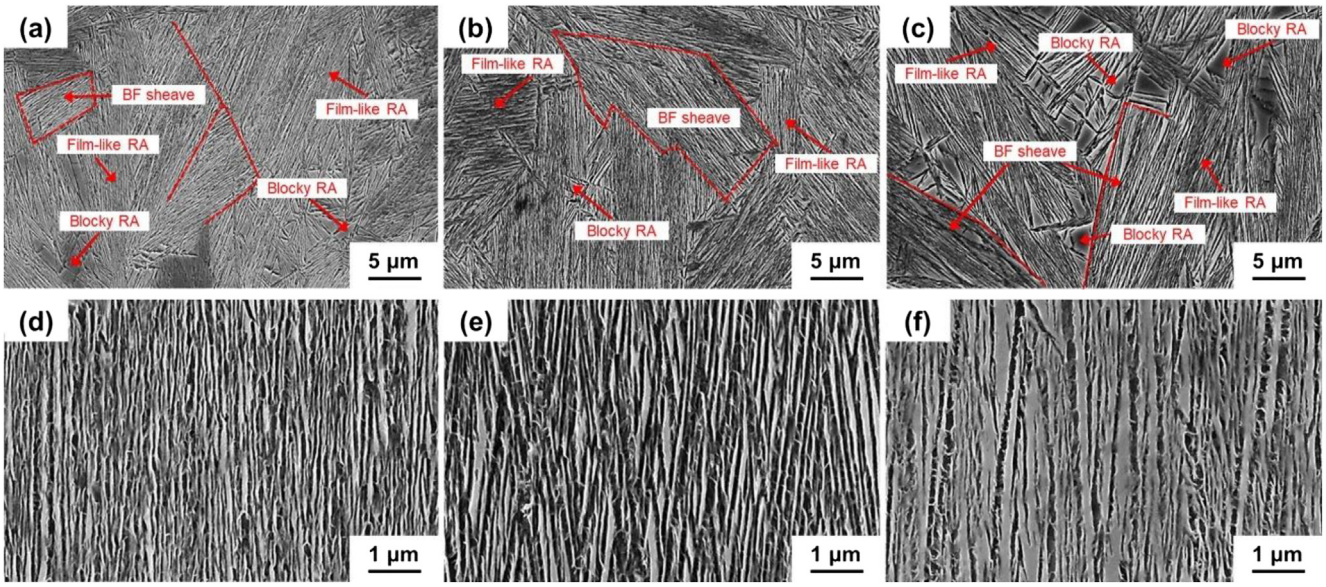

Fig. 8 – SEM images of the studied steel after austempering by different processes: (a,d) 210 °C-83 h; (b,e) 240 °C-33 h; (c,f) 270 °C-11 h.

the cooling process, a significant amount of austenite transforms into martensite, resulting in a low RA content at room temperature. However, as the bainite transformation continues, the supersaturated C atoms in the new phase diffuse into the surrounding austenite, and the presence of Si and Al inhibits the precipitation of carbides, leading to an increase in the carbon content and enhanced stability of the parent phase. Consequently, there is a reduction in the amount of martensite transformation during subsequent cooling, allowing for the retention of more RA. Following the peak of RA content, there is a decrease in RA content with continued austempering. This can be attributed to the fact that, after a sufficiently long holding time, the free energy of austenite would become smaller than that of bainite with the same composition when the carbon concentration in austenite reaches a level where further diffusion transition becomes thermodynamically impossible [32]. Insufficient bainite nucleation conditions contribute to lower values of RA content once again. In addition, as the austempering temperature decreases, the RA content reduces slightly when the bainite transformation is complete. This is due to the larger driving force of phase transformation at lower temperatures, coupled with the slowed diffusion of carbon atoms into the parent phase, resulting in a higher degree of phase transformation and a subsequent decrease in untransformed austenite content.

Fig. 8 shows the SEM images of the studied steel after austempering at 210 °C, 240 °C and 270 °C. In all cases, the microstructures consist of numerous bainite ferrite sheaves with a disordered distribution. More specifically, each sheaf consists of many elongated bainite laths with film-like austenite distributed between them. The orientation of the laths is consistent with that of the sheaf. Besides the film-like austenite located between the bainite laths, there is also blocky austenite distributed at the junction of sheaves, both of which have significantly distinct microstructure and size. Fig. 9 shows the TEM images of the studied steel after

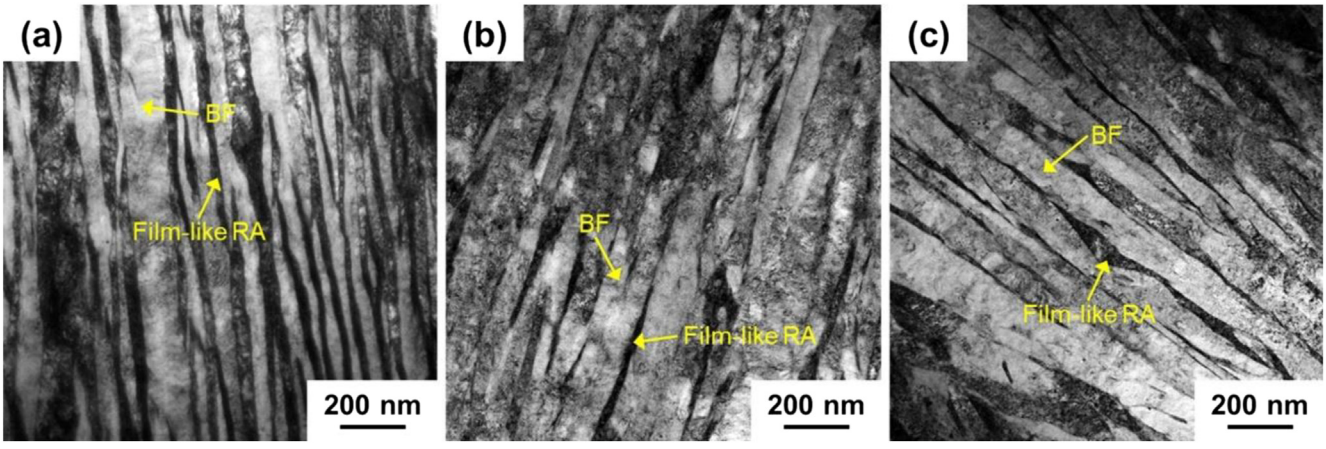

Fig. 9 – TEM images of the studied steel after austempering by different processes: (a) 210 °C-83 h; (b) 240 °C-33 h; (c) 270 °C-11 h.

austempering. The nano-bainite laths and film-like austenite are distributed alternately and almost parallel. Such bainite is different from the conventional upper bainite or lower bainite with carbides precipitation, and belongs to a novel carbide-free nano-bainite microstructure, known as super bainite, as termed by Bhadeshia et al. [33]. The mean linear intercept method is applied to determine the thickness of bainite laths in high magnification SEM and TEM images using Image-Pro Plus software. Any errors induced in the measurement are corrected according to the following equation [34]:

$$L_T = \pi t / 2 \quad (2b)$$

where L_T is the measured thickness of lath, t is the actual value of thickness, the statistical results are shown in Table 2. It is found that the thickness of bainite ferrite laths decreases progressively with a lower austempering temperature. The elevated subcooling level enhances the driving force for phase transformation, resulting in a higher rate of bainite nucleation. Furthermore, the shear resistance of supercooled austenite at lower temperatures is large, and the growth of bainite is hard, all of which collectively contribute to the formation of thinner bainite ferrite laths obtained austempering at lower temperatures, even less than 100 nm.

3.2. *Effect of austempering temperature on mechanical properties*

Fig. 10(a) shows that the Brinell hardness of the studied steel after different austempering processes decreases first and then increases with prolonged austempering time. The bainite transformation of the short-time austempering is not sufficient, and the high carbon martensite formed during cooling contributes to higher hardness. As the austempering time extends, the content of bainite and retained austenite at room temperature increases, resulting in a sharp drop in hardness. Subsequently, with the disappearance of martensite and the decrease in RA content, the hardness gradually recovers due to ongoing bainite transformation. Compared the hardness after bainite transformation, the Brinell hardness after austempering at 270 °C, 240 °C and 210 °C reached approximately 554 HBW, 579 HBW and 615 HBW, respectively. This is primarily attributed to the reduced RA content and the slower diffusion of C atoms at low temperatures. The increased presence of supersaturated carbons is retained in the bainite, allowing for an increase of the matrix hardness. In addition, the interphase structure of ultrafine (sub-micron or nano-scale) bainite laths and film-like austenite plays a crucial role in achieving high hardness. The finer bainite laths obtained at lower temperatures contribute to the overall improvement in hardness.

Table 2 – Measured and actual thickness of bainite ferrite laths.

Process	L_T/nm	t/nm
270 °C-11 h	~170	~110
240 °C-32 h	~135	~85
210 °C-83 h	~90	~60

The tensile properties of the studied steel are shown in Fig. 10(b). The yield strength (YS) and tensile strength after austempering at 210 °C can reach 1743 MPa and 2099 MPa, respectively, but the total elongation is limited to 5.4%, resulting in a product of strength and elongation (PSE) of approximately 11.3 GPa%. When the austempering temperature rises to 240 °C, the tensile strength remains high at 1996 MPa, while the total elongation improves to 9.2%, resulting in an increased PSE of approximately 18.4 GPa%. Further raising the austempering temperature to 270 °C, the tensile strength decreases to 1779 MPa, but the total elongation surprisingly increases to 16.24%, reaching the maximum value of around 28.8 GPa%. The ultra-high strength of the studied steel is primarily attributed to the ultra-fine microstructure of the bainite laths and film-like austenite as well as the dislocation strengthening produced by the high density of dislocations [35]. It should be noted that the content and morphology of RA in the nano-bainite structure have a great effect on plasticity. The presence of film-like austenite can induce crack bifurcation or effectively prevent crack propagation, thereby improving the plasticity. On the other hand, the blocky austenite distributed between the sheaves has an uneven distribution of carbon. This affects the mechanical stability of austenite, reduces the ability for coordinated deformation, and promotes its transformation into brittle martensite, resulting in less noticeable improvement in plasticity.

Fig. 11 shows the tensile fracture morphology under different austempering processes, characterized by the presence of dimples and tearing edges. The fracture surface after austempering at 210 °C is relatively flat, exhibiting minimal dimpling, and still retains the metal luster after machining. After austempering at 240 °C, a few shallow dimples can be observed in the fracture, although tearing edges still dominate, and the metal luster on the fracture surface is dim. Notably, when the austempering temperature is set at 270 °C, the fracture surface exhibits significant undulations with distinct deep dimples and tearing edges caused by plastic deformation. The fracture surface shows uneven fibrous texture, and the metal luster completely disappears.

3.3. *Effect of austempering temperature on wear resistance*

Fig. 12(a) shows the pin-on-disc wear weight loss, and the corresponding hardness of the studied steel under different austempering processes. With the decrease of austempering temperature, the hardness of nano-bainite increases, resulting in a reduction in the weight loss and an improvement in the wear resistance of pin-on-disc wear. During the wear process of metal materials, the surface is subjected to a certain depth of structural change due to the influence of load and friction heat. Typically, after the wear of high-strength martensitic steels, the heat generated during the wear process softens the structure, causing a decrease in surface hardness and consequently deteriorating the wear resistance, as tempered martensite is more sensitive to temperature [36]. However, nano-bainite exhibits superior tempering stability, effectively mitigating the above phenomenon [37]. Fig. 13 shows the surface morphology of the sample after a low

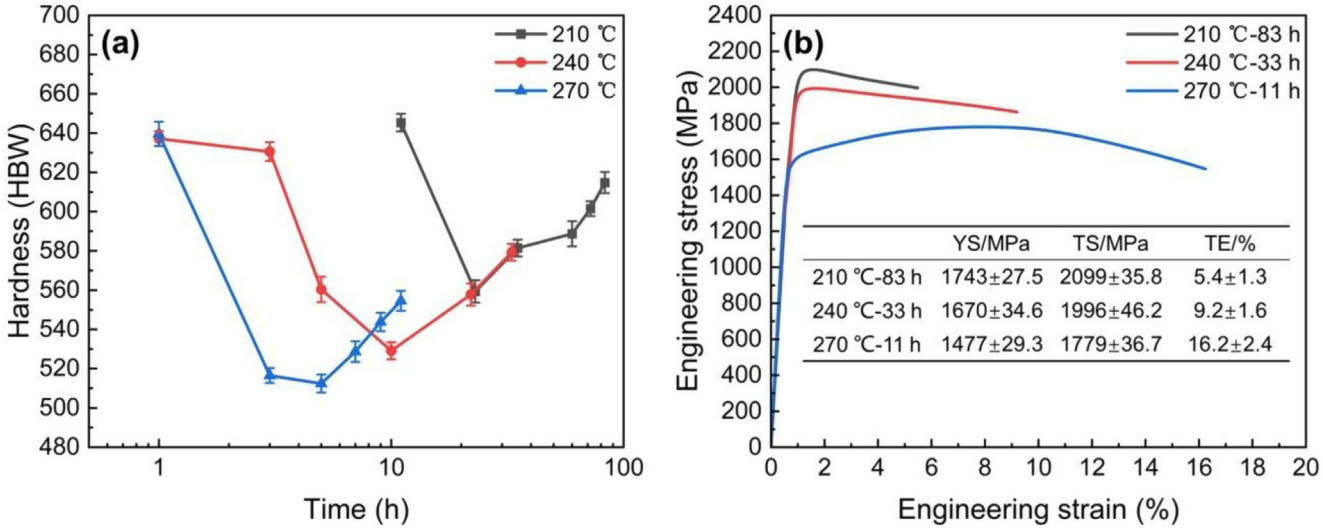

Fig. 10 – Studied steel properties after different austempering by different processes: (a) Brinell hardness; (b) engineering stress-strain curves.

stress pin-on-disc wear test. When the sample has low hardness and good plasticity, the abrasive particles penetrate deeper, and the metal bulged on both sides of the groove is pushed or cut by abrasive particles to deform plastically, which forms a flake-like strip. In the subsequent abrasive wear process, the flake-like strip is detached after repeated plastic deformation, and the arrow in Fig. 13(c) shows the side wall stripping. Moreover, due to the deep indentation of the abrasive particles, metal accumulation is likely to occur, leading to increased sliding resistance of the abrasive particles. The secondary wear occurs by abrasive particles crushing, so that the grinding marks deviating from the wear direction appear in the wear morphology, and the ellipse in the figure shows the abrasive particle penetration. As shown in Fig. 13(a and b), the higher hardness of the sample surface makes the abrasive particles be pressed into a shallow depth, following the formation of flatter grooves and fewer prominent flake-like strips, which indicates that with the increase of hardness, the probability of abrasive particle breakage decreases, which reduce the wear loss caused by the secondary wear.

Fig. 12(b) shows the weight loss curves of the samples after undergoing different austempering processes in the impact wear test. There is a pronounced difference in the weight loss from about 1 h. The curves of 240 °C-32 h and 210 °C-83 h exhibit a predominantly linear trend, while the slope of 270 °C-11 h sample becomes slower in terms of improved wear resistance. The impact wear resistance characteristics of the samples are intimately relevant to their comprehensive mechanical properties. The 270 °C-11 h sample with the optimal strength and plasticity match shows excellent impact wear resistance. The surface morphology after impact wear for 1.5 h is shown in Fig. 14(a–c), which mainly includes abrasive particle penetration, micro cutting, and plastic deformation. The regular impact of the upper and lower samples can press the abrasive particles flowing through the middle into the wear surface, which in turn squeezes the surrounding metal and produces consequent plastic deformation.

The long-term erosion of the abrasive particles and the relative sliding of the upper and lower samples cause the formation of micro-cutting on the surface, which likewise induces plastic deformation. In the case of the 270 °C-11 h sample with the optimal strength and plasticity match, the abrasive particles produce long shallow cuts under the horizontal component force. The metal surrounding the abrasive particles is either pushed to both sides of the cuts or directly

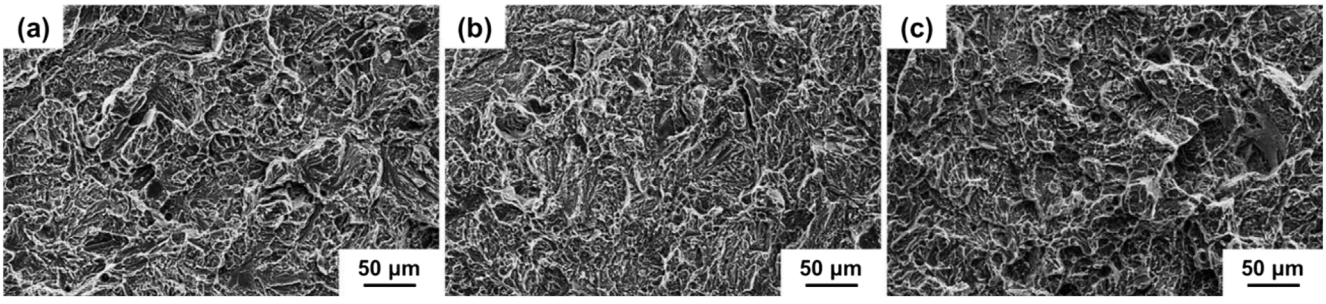

Fig. 11 – Fracture morphology of the studied steel after austempering by different processes: (a) 210 °C-83 h; (b) 240 °C-33 h; (c) 270 °C-11 h.

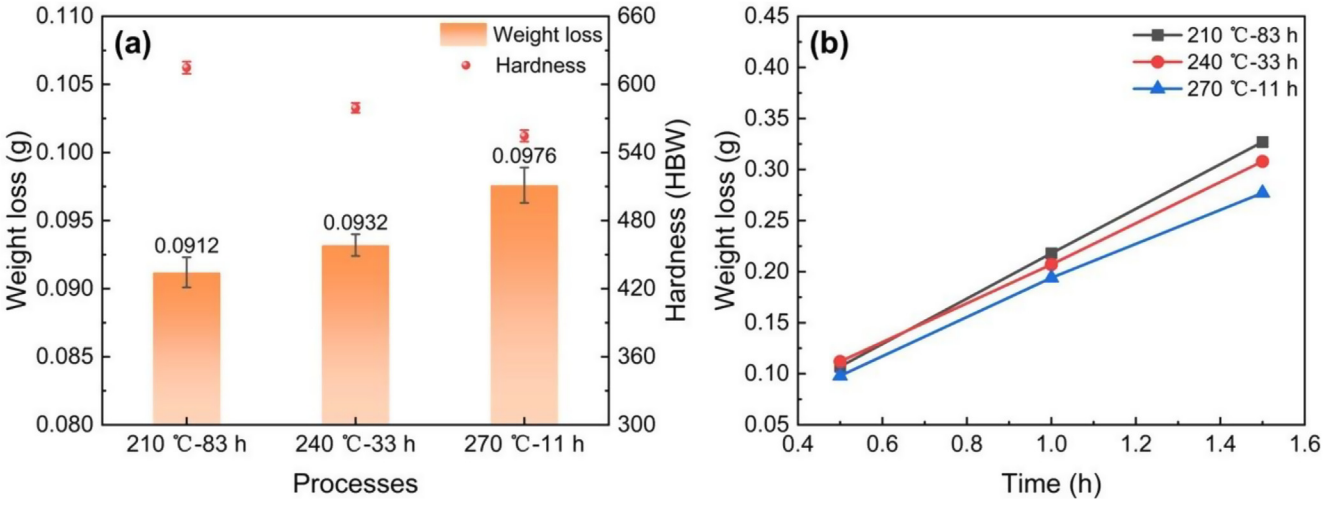

Fig. 12 – (a) Pin-on-disc wear weight loss; (b) impact wear weight loss curves of the studied steel.

displaced, leading to localized plastic deformation, as shown in Fig. 14(c). Micro-cutting is the evidence of plastic deformation in the micro area. Regardless of the length of cuts, the wear surface tends to undergo local plastic deformation, and the deformed metal suffers fatigue shedding due to the continuous abrasive particles' effect and thus weight loss. Whereas the fragmentation and detachment triggered by the abrasive particles' penetration seems to be an entirely brittle process, as shown in Fig. 14(a and b). It should be pointed out that all the observations of the wear morphology are static after the end of the wear, showing an instantaneous state. Therefore, micro-cutting cannot occur continuously at a certain position on the surface (such as the position where cutting is observed). It is possible that the cutting on the surface is only created by the abrasive particles when the wear test approaches its end. During dynamic impact, the fragmentation and detachment caused by micro-cutting and abrasive particles penetration interact. The damage cracks on the subsurface of impact wear samples have different forms and causes.

4. Discussions

4.1. *Relationship between retained austenite and mechanical properties in carbon-free nano-bainite steel*

In the XRD patterns, the diffraction peaks of austenite before and after tension have different intensity changes, among which the intensity of (220)γ peak is almost unchanged after tension, while the intensity of (200)γ and (311)γ peaks after tension exhibits different changes in samples (Fig. 15(a)). The intensity of (200)γ and (311)γ peaks decreases significantly after tension for the austempered sample at 270 °C, while the intensity changes of (200)γ and (311)γ peaks are less pronounced in austempered sample at 210 °C. The diffraction peaks of ferrite show similar trends in intensity change after tension, with minimal variation in the intensity of (200)α peak and a slight increase in the intensity of the (211)α peak. The austenite content of the studied steels shows different magnitudes of reduction after tension (Fig. 15(b)). For the samples

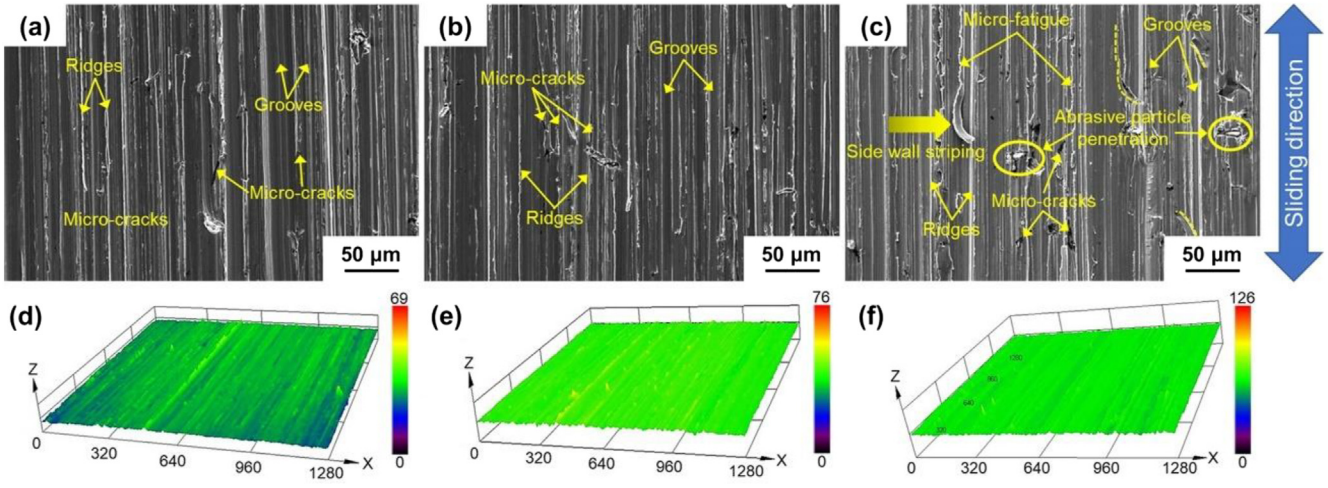

Fig. 13 – Surface morphology and 3D reconstructions of the studied steel after pin-on-disc wear: (a,d) 210 °C-83 h; (b,e) 240 °C-33 h; (c,f) 270 °C-11 h.

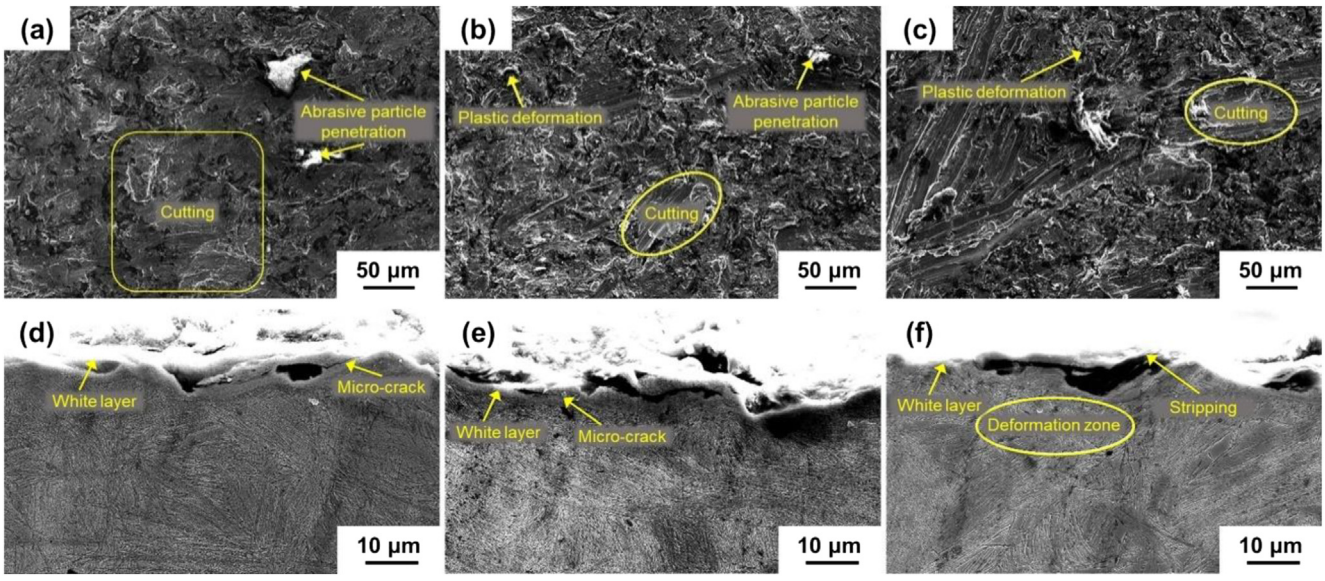

Fig. 14 – Surface and subsurface morphology of the studied steel after impact wear: (a,d) 210 °C-83 h; (b,e) 240 °C-33 h; (c,f) 270 °C-11 h.

after austempering at 270 °C and 240 °C, the austenite content decreases from 34.8% to 26.7% and from 34.5% to 29.3%, respectively, while for the sample after austempering at 210 °C, the austenite content only decreases by 3.6%. The secondary deformation mechanisms such as transformation-induced plasticity (TRIP) or twinning-induced plasticity (TWIP) tend to dominate in composition systems with low stacking fault energy (SFE) [38]. According to the analysis of XRD results, the austenite content decreases the most after austempering at 270 °C, indicating a more complete progression of the TRIP effect. The variations in austenite content reflect the differences of tensile properties, especially in elongation, but this is not the sole determining factor. Compared with BF, due to the low SFE of RA, it plays a coordinating role in the deformation process of nano-bainite steel. In fact, the influence of RA content and its mechanical stability on the TRIP effect is an important reason for the prominent difference in plasticity.

As a rule, the mechanical stability of RA can be calculated by the equation based on the OC model [39,40]:

$$K\varepsilon = -\ln\left(\frac{V_\gamma}{V_{\gamma 0}}\right) \tag{4}$$

where K is the mechanical stability of RA, ε is the strain, $V_{\gamma 0}$ is the initial RA content, and V_γ is the RA content after tension. The lower the K value, the higher the mechanical stability of RA. In the current experimental range, the carbon content in RA increases from 1.35 wt% to 1.70 wt%, while the K value decreases from 2.22 to 1.64 with the increase of austempering temperature (Fig. 15(c)). The higher mechanical stability of RA in the austempered sample at 270 °C can be attributed to its higher carbon content in RA in addition to the thinned film-like RA [41,42]. During the tensile process, austenite undergoes phase transformation when the stress provides additional driving force, reducing the stress concentration caused by plastic deformation. From the previous microstructure analysis, it is evident that the nano-bainite steels prepared in this study are dominated by film-like RA, and only a very small amount of blocky austenite with poor mechanical stability is present. The film-like austenite gradually transforms to martensite, and the per unit plastic percentage transformed from RA is much lower than that of blocky austenite [43]. Additionally, unlike the incoherent interface between multiple phases, transformed martensite and unconverted austenite satisfy the Kurdjumov-Sachs (K–S) orientation relationship, which facilitates the movement of dislocations from martensite to adjacent austenite [44]. This dislocation movement can promote the synergistic deformability of the two phases to produce sustained plastic deformation, resulting in sustained plastic deformation without inducing crack initiation at the interface [45]. The austempered sample at 270 °C, which contains a higher proportion of film-like RA with greater mechanical stability, exhibits optimal plasticity along with the progressive phase transformation.

4.2. *Wear mechanism in carbon-free nano-bainite steel*

The 3D reconstructed morphology of the surface after pin-on-disc wear shows that the surface morphology of the 270 °C-11 h sample after wear is the flattest since the highest hardness makes it difficult for the abrasive particles to press in, so the wear track is wide and shallow (Fig. 13(d–f)). On the other hand, the bulging metal is prone to be broken owing to poor plasticity, which also promotes the flatness of the wear surface. The wear surfaces of the 240 °C-33 h sample and the 210 °C-83 h sample exhibit more fluctuating patterns because of the lower hardness of the samples and the deeper indentation of the abrasive particles, forming deep and narrow wear tracks. The continuous wear makes the higher ridges more susceptible to severe plastic deformation resulting in fatigue fracture of the material and increased weight loss. The mechanisms involved in pin-on-disc wear are mainly in the

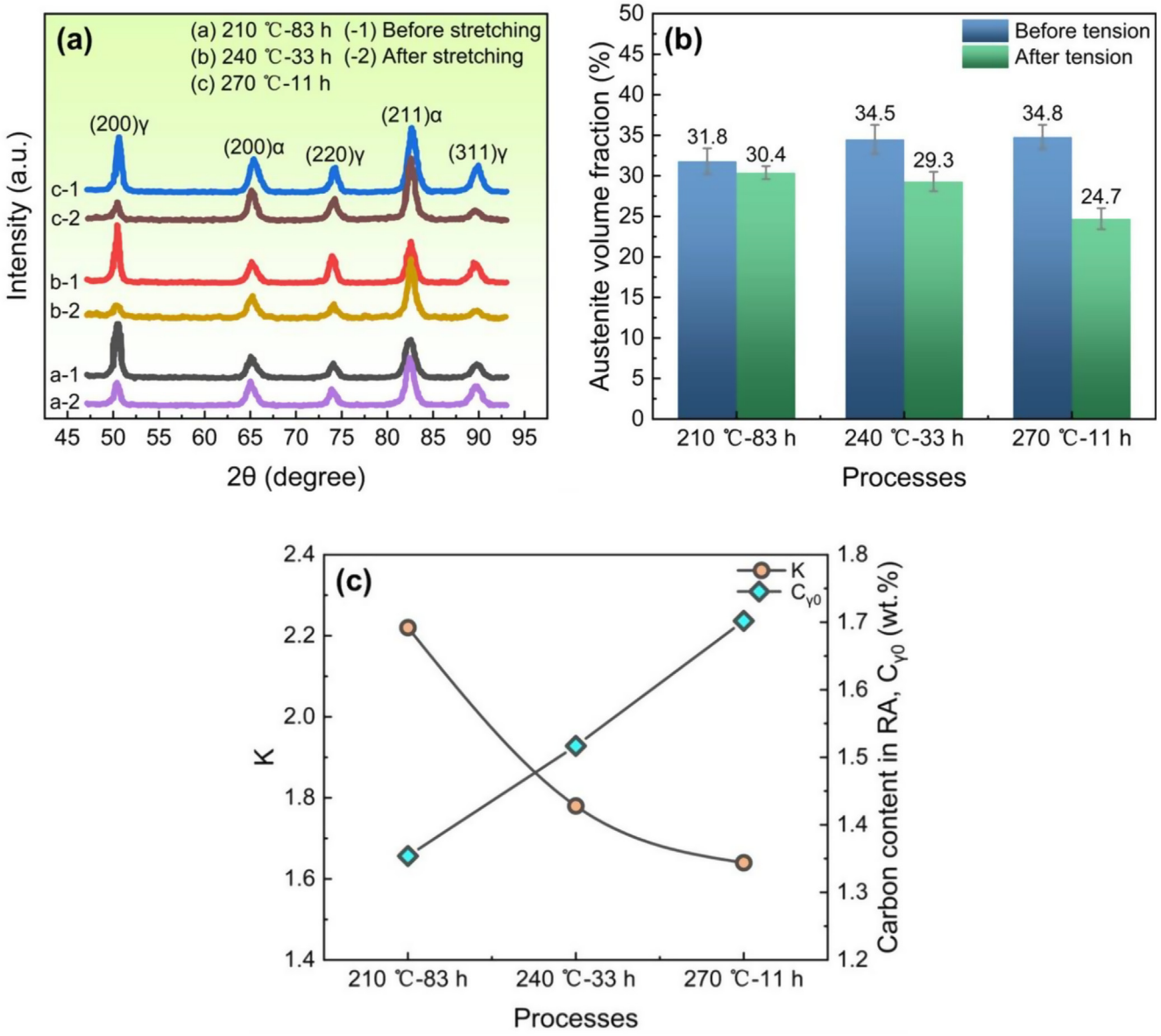

Fig. 15 – (a) XRD patterns of the studied steel at different processes; (b) changes of austenite volume fraction over time at different austempering temperatures before and after tension; (c) carbon content and mechanical stability of RA.

form of micro-cutting, micro-ploughing and micro-fatigue [46]. When the abrasive particles are in contact with the wear surface at an angle, the micro-cutting leads to the removal of a layer of metal in the form of chips [47]. As can be seen from the surface micromorphology shown in Fig. 13, fine shear bands are formed in the grooves caused by micro-cutting, due to work hardening as a result of highly concentrated and uneven strain in narrow areas [48]. Deformation-induced martensite phase transformation can take place in the shear bands, where fresh martensite as a brittle phase inhibits microcutting, but also reduces deformability. For the ultra-high strength nano-bainite steels in this study, in most cases, the abrasive particles do not always cut through the surface and embed, but rather generate ridges on both sides of the grooves via micro-ploughing mechanism [49]. By sliding relatively without interruption under constant pressure stress, the micro-fatigue mechanism causes some of the metal to strip at the side wall on the ridges. The micro-cracks and secondary wear on the wear surface are caused by a combination of adhesion and micro-fatigue mechanisms. The broken abrasive particles or shedding metal may adhere to the wear surface, forming micro-cracks perpendicular to the sliding direction or shifting the wear track under low cycle fatigue, especially for steels with low hardness [50]. Overall, the micro-cutting mechanism in pin-on-disc wear leads to significant wear weight loss, while the micro-ploughing and micro-fatigue mechanisms are milder. In the case of similar RA content, for the carbide-free nano-bainite steel with high hardness obtained by austempering at 210 °C, the RA with poor mechanical stability accelerates the transformation of metastable austenite to martensite. This not only reduces the penetration depth of abrasive particles but also increases the

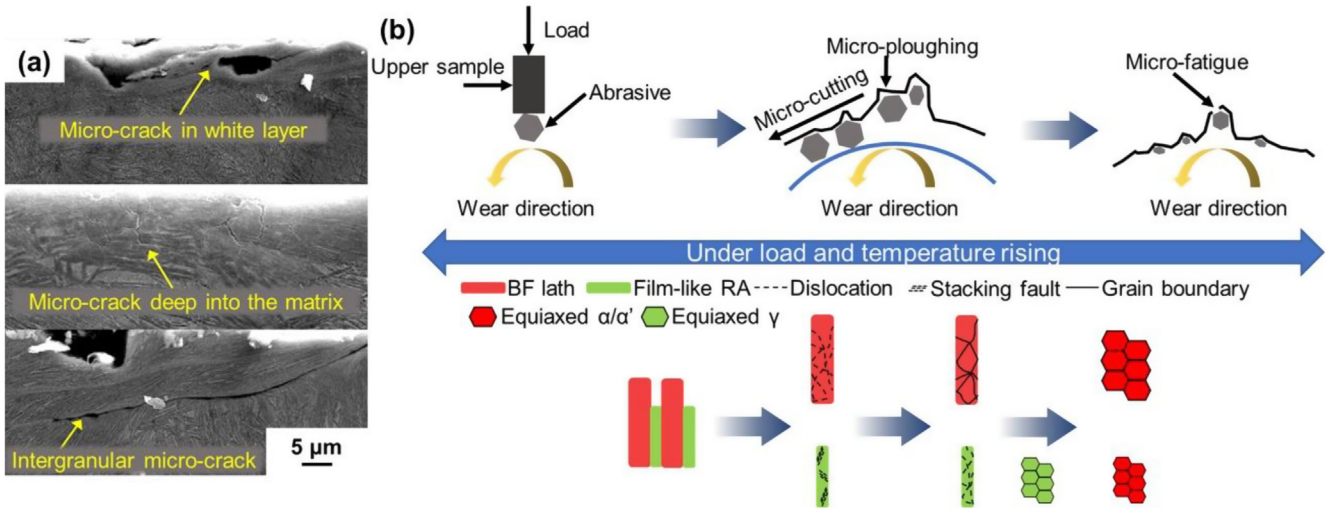

Fig. 16 – (a) Various types of cracks in the subsurface; (b) schematic diagram of impact wear of carbide-free nano-bainite steel.

resistance of micro-crack initiation. Additionally, the crack tip experiences compressive stress and undergoes passivates due to volume expansion.

The subsurface after impact wear of the 270 °C-11 h sample exhibits significant deformation, reaching a depth of approximately 30 μm, while the subsurface deformation of the 210 °C-83 h sample is minimal, with a depth of about 10 μm (Fig. 14(d–f)). The subsurface morphology consists of the characteristic white layer and the plastic deformation zone. The white layer is the zone near the wear surface that is resistant to erosion and appears bright under electron microscopy. Its formation is attributed to the combined effects of frictional heat and strain induced processes [51]. Under the impact load, the temperature of the surface rises due to deformation, and local softening and strain accumulation occur simultaneously. When the softening effect exceeds the strain hardening effect, the local deformation of the surface continues to develop, resulting in the formation of white layer [52]. The white layer is loose, and some parts retain cracks extending from the wear surface into the subsurface, which expand until cross-linking with each other causing the stratification. The white layer is easily peeled off and causes weight loss during the subsequent wear process. Conversely, the microstructure near the plastic deformation zone is dense, and its depth depends on the material properties and impact conditions.

When the strain reaches saturation due to the repeated impacts, cracks are generated as a means of releasing energy. Continued application of load leads to crack propagation, resembling a rapid fatigue process [53]. The cracks are closely associated with high-speed strain concentration during impact wear, initiating when the strain cannot be effectively accommodated. The cracks tend to propagate along the 45° direction (maximum shear strain in the 45° direction) and gradually extend to the horizontal direction (Fig. 16(a)). Eventually, when the cracks intersect, the stripping is triggered. When the cracks penetrate into the plastic deformation zone, the deeper the micro-crack penetrates into the matrix, the smaller it is, and the crack direction starts to show multi-directionality, indicating obstruction in their advancement into the matrix. Due to the different deformation rates of the white layer and the plastic deformation zone, the crack initiates between them and propagates along the grain boundaries in the process of continuous impact, and the microstructure of both the upper and lower regions of the crack undergoes evident deformation. This is because the stress concentration at the grain boundary facilitates the crack propagation, while the deformation of the intracrystalline prevents the crack from propagating into the grain.

The weight loss of impact wear predominantly arises from shedding caused by fatigue failure. The accumulation of plastic deformation results in a large number of dislocation plugging, which inevitably leads to the formation of micro-cracks. Fig. 16(b) depicts the schematic diagram of impact wear of carbide-free nano-bainite steel. The phase interfaces, grain boundaries, and defects of nano-bainite steel are susceptible to act as initiation sites for cracks. The plastic deformation of the microstructure consumes a portion of the impact energy, thereby influencing the impact wear resistance [54]. The effect of different austempering temperatures on the thickness of bainite laths and film-like austenite contributes to the ability to coordinate the deformation. In turn, the content and mechanical stability of RA largely play a significant role in determining the plasticity of the nano-bainite steel. With the increase of austempering temperature, the strength-plasticity matching of nano-bainite steel is improved. It should be noted that, unlike pin-on-disc wear, the progressive TRIP effect from the increased content and mechanical stability of RA effectively prevents crack propagation which contributes to the impact wear resistance.

5. Conclusions

In summary, the effect of austempering temperature on the microstructure and mechanical properties of carbide-free nano-bainite steels was studied. The wear characteristics of carbide-free nano-bainite steels were investigated by low

stress pin-on-disc wear and dynamic load impact wear tests. The relationship between the content and mechanical stability of RA and the strength-plasticity matching was analyzed. The wear mechanisms of carbide-free nano-bainite steel and the role played by RA in it were emphatically discussed. The main conclusions are as follows.

(1) The phase transformation rate of bainite is affected by carbon diffusion. The completion time of phase transformation at 270 °C, 240 °C and 210 °C is 7.8 h, 28.4 h and 80 h, respectively. The phase transformation incubation period of bainite is prolonged and the phase transformation rate slows down as austempering temperature decreases, but the degree of phase transformation increases. The highest strength and hardness of 2099 MPa and 615 HBW, respectively, are achieved after austempering at 210 °C for 83 h. After austempering at 270 °C for 11 h, the best matching of strength and plasticity is obtained, and the product of strength and plasticity is 28.8 GPa%, which can be attributed to the presence of more film-like RA with high mechanical stability.
(2) The dominant wear mechanism of pin-on-disc wear is micro-cutting, resulting in significant weight loss, while micro-ploughing and micro-fatigue mechanisms are milder. For the high hardness carbide-free nano-bainite steel obtained by austempering at 210 °C, RA with poor mechanical stability accelerates the transformation of metastable austenite to martensite. While reducing the penetration depth of the abrasive particles, the propagation resistance of the micro-crack tip is increased.
(3) The wear mechanisms of impact wear include abrasive particles penetration, micro-cutting and plastic deformation, where fatigue failure due to plastic deformation is the main reason for weight loss. The dominant factor affecting wear resistance is the strength-plasticity match, and the 270 °C-11 h sample with the highest PSE has the best impact wear resistance. Unlike pin-on-disc wear, the progressive TRIP effect from the increased RA content and mechanical stability effectively inhibits crack propagation.

Declaration of competing interest

The authors declare that they have no known competing financial interests or personal relationships that could have appeared to influence the work reported in this paper.

Acknowledgements

E.M. Wang, H.B. Wu and G. Niu appreciate the support from the National Natural Science Foundation of China (Grant Nos. 51774033 and 51474031). G. Niu appreciates the support from the China Postdoctoral Science Foundation (2022M720402). Thanks to Professor Misra for review and editing.

REFERENCES

[1] Holmberg K, Kivikytö-Reponen P, Härkisaari P, Valtonen K, Erdemir A. Global energy consumption due to friction and wear in the mining industry. Tribol Int 2017;115:116–39.
[2] Gola AM, Ghadamgahi M, Ooi SW. Microstructure evolution of carbide-free bainitic steels under abrasive wear conditions. Wear 2017;376–377:975–82.
[3] Miab SA, Avishan B, Yazdani S. Wear resistance of two nanostructural bainitic steels with different amounts of Mn and Ni. Acta Metall Sin 2016;29:587–94.
[4] Yang J, Wang TS, Zhang B, Zhang FC. Sliding wear resistance and worn surface microstructure of nanostructured bainitic steel. Wear 2012;282–283:81–4.
[5] Dong HY, Wu KM, Wang XL, Hou TP, Yan R. A comparative study on the three-body abrasive wear performance of Q&P processing and low-temperature bainitic transformation for a medium-carbon dual-phase steel. Wear 2018;402–403:21–9.
[6] Chattopadhyay C, Sangal S, Mondal K, Garg A. Improved wear resistance of medium carbon microalloyed bainitic steels. Wear 2012;289:168–79.
[7] Hofer C, Winkelhofer F, Clemens H, Primig S. Morphology change of retained austenite during austempering of carbide-free bainitic steel. Mater Sci Eng, A 2016;664:236–46.
[8] Zhang P, Chen JX, Li J, Yu HL, Tu XH, Li W. Microstructure evolution mechanism of carbides-free bainite steel during impact abrasive wear. Wear 2021:486–7.
[9] Rogal L, Solano-Alvarez W, Szklarz Z, Bhadeshia HKDH. Feasibility study for thixoforming nanostructured bainitic steels. Mater Sci Eng, A 2016;651:708–19.
[10] Suikkanen PP, Cayron C, DeArdo AJ, Karjalainen LP. Crystallographic analysis of isothermally transformed bainite in 0.2C-2.0Mn-1.5Si-0.6Cr steel using EBSD. J Mater Sci Technol 2013;29:359–66.
[11] Yoozbashi MN, Yazdani S, Wang TS. Design of a new nanostructured, high-Si bainitic steel with lower cost production. Mater Des 2011;32:3248–53.
[12] Liu W, Liang J, Jiang Y, Zhang B, Zhao A. A study of blocky retained austenite and properties under variously heat-treated ultra-fine bainitic steel. Mater Res Express 2019;6:0–11.
[13] Hasan HS, Peet MJ, Avettand-Fènoël MN, Bhadeshia HKDH. Effect of tempering upon the tensile properties of a nanostructured bainitic steel. Mater Sci Eng, A 2014;615:340–7.
[14] Zhao J, Lv B, Zhang F, Yang Z, Qian L, Chen C, et al. Effects of austempering temperature on bainitic microstructure and mechanical properties of a high-C high-Si steel. Mater Sci Eng, A 2019;742:179–89.
[15] Tian J, Xu G, Jiang Z, Zhou M, Hu H, Yuan Q. Transformation behavior of bainite during two-step isothermal process in an ultrafine bainite steel. ISIJ Int 2018;58:1875–82.
[16] Lee SI, Lee JM, Kim SG, Song YB, Kim HK, Shim JH, et al. Influence of austempering temperature on microstructure and mechanical properties of high-carbon nanostructured bainitic steels. Mater Sci Eng, A 2022;848:143334.
[17] Qin Y man, bo Liu C, Zhang C, Sheng, biao Wang X, yan Long X, guo Li Y, et al. Comparison on wear resistance of nanostructured bainitic bearing steel with and without residual cementite. J Iron Steel Res Int 2022;29:339–49.
[18] Du Y, Wang X, Zhang D, Wang X, Ju C, Jiang B. A superior strength and sliding-wear resistance combination of ductile iron with nanobainitic matrix. J Mater Res Technol 2021;11:1175–83.

[19] Luo QS, Mei HJ, Kitchen M, Gao YB, Bowen L. Effect of short-term low-temperature austempering on the microstructure and abrasive wear of medium-carbon low-alloy steel. Met Mater Int 2021;27:3115–31.
[20] Ríos-Diez O, Aristizábal-Sierra R, Serna-Giraldo C, Eres-Castellanos A, García-Mateo C. Wear behavior of nanostructured carbo-austempered cast steels under rolling-sliding conditions. J Mater Res Technol 2021;11:1343–55.
[21] Xu Z. Capability of nodular eutectic and austenite-bainite polyphase structure to resist impact abrasive wear. Wear 2002;253:597–603.
[22] Narayanaswamy B, Hodgson P, Timokhina I, Beladi H. The impact of retained austenite characteristics on the two-body abrasive wear behavior of ultrahigh strength bainitic steels. Metall Mater Trans A Phys Metall Mater Sci 2016;47:4883–95.
[23] Koyama M, Zhang Z, Wang M, Ponge D, Raabe D, Tsuzaki K, et al. Bone-like crack resistance in hierarchical metastable nanolaminate steels. Science 2017;355(80):1055–7.
[24] Bhadeshia HKDH. The first bulk nanostructured metal. Sci Technol Adv Mater 2013;14.
[25] Avishan B, Garcia-Mateo C, Yazdani S, Caballero FG. Retained austenite thermal stability in a nanostructured bainitic steel. Mater Char 2013;81:105–10.
[26] Bhuyan D, Sastry GVS, Patra S, Pradhan SK, Manna R. Effect of austempering time on bainite plate thickness and variant selection in a high carbon low alloy steel. Mater Char 2023;200:112923.
[27] Long XY, Kang J, Lv B, Zhang FC. Carbide-free bainite in medium carbon steel. Mater Des 2014;64:237–45.
[28] Lonardelli I, Bortolotti M, Van Beek W, Girardini L, Zadra M, Bhadeshia HKDH. Powder metallurgical nanostructured medium carbon bainitic steel: kinetics, structure, and in situ thermal stability studies. Mater Sci Eng, A 2012;555:139–47.
[29] Guo Hui, Zhou Peng, Zhao Ai-min, Zhi Chao, Ran Ding JW. Effects of Mn and Cr contents on microstructures and mechanical properties of low temperature bainitic steel. J Iron Steel Res Int 2017;21:290–5.
[30] Beladi H, Timokhina IB, Hodgson PD, Adachi Y. Characterization of nano-structured bainitic steel. Int J Mod Phys Conf Ser 2012;5:1–8.
[31] Guo H, Gao G, Gui X, Misra RDK, Bai B. Structure-property relation in a quenched-partitioned low alloy steel involving bainite transformation. Mater Sci Eng, A 2016;667:224–31.
[32] Caballero FG, Garcia-Mateo C, Santofimia MJ, Miller MK, García de Andrés C. New experimental evidence on the incomplete transformation phenomenon in steel. Acta Mater 2009;57:8–17.
[33] Mawella KJA, Caballero FG, Bhadeshia HKDH. Bainitic steel. US 6884306 B1; 2005.
[34] Garcia-Mateo C, Caballero FG, Bhadeshia HKDH. Acceleration of low-temperature bainite. ISIJ Int 2003;43:1821–5.
[35] Yu X, Wu H, Zhang Y, Yuan R, Gu Y, Feng Y. Influence of niobium microalloying on the thermal stability of medium-carbon carbide-free bainitic steel. J Mater Res Technol 2021;12:487–99.
[36] Liu W, Jiang Y, Liu H, Zhao A. A study of wear resistance of carbon-free bainite and martensite in medium carbon steel. Ironmak Steelmak 2020;47:1056–62.
[37] Wang K, Gui X, Bai B, Gao G. Effect of tempering on the stability of retained austenite in carbide-free bainitic steel. Mater Sci Eng, A 2022;850:143525.
[38] Pierce DT, Jiménez JA, Bentley J, Raabe D, Wittig JE. The influence of stacking fault energy on the microstructural and strain-hardening evolution of Fe-Mn-Al-Si steels during tensile deformation. Acta Mater 2015;100:178–90.
[39] Wang X, Zhang X, Fang Q, Ma H, Zhang R, Liu F, et al. Effect of tempering on stability of retained austenite and tensile properties of nanostructured bainitic steel. Mater Sci Eng, A 2022;856:143958.
[40] Li ZC, Ding H, Cai ZH. Mechanical properties and austenite stability in hot-rolled 0.2C-1.6/3.2Al-6Mn-Fe TRIP steel. Mater Sci Eng, A 2015;639:559–66.
[41] Saha Podder A, Bhadeshia HKDH. Thermal stability of austenite retained in bainitic steels. Mater Sci Eng, A 2010;527:2121–8.
[42] Wang F, Qian D, Hua L, Xie L. Tempering response and improved mechanical properties in secondary hardened steel by introducing an optimized austempering process. Mater Sci Eng, A 2021;807:140895.
[43] Shen YF, Qiu LN, Sun X, Zuo L, Liaw PK, Raabe D. Effects of retained austenite volume fraction, morphology, and carbon content on strength and ductility of nanostructured TRIP-assisted steels. Mater Sci Eng, A 2015;636:551–64.
[44] Zhou Q, Qian L, Meng J, Zhao L. The fatigue properties, microstructural evolution and crack behaviors of low-carbon carbide-free bainitic steel during low-cycle fatigue. Mater Sci Eng, A 2021;820:141571.
[45] Zhao P, Zhang B, Cheng C, Misra RDK, Gao G, Bai B, et al. The significance of ultrafine film-like retained austenite in governing very high cycle fatigue behavior in an ultrahigh-strength MN-SI-Cr-C steel. Mater Sci Eng, A 2015;645:116–21.
[46] Moghaddam PV, Rinaudo M, Hardell J, Vuorinen E, Prakash B. Influence of fracture toughness on two-body abrasive wear of nanostructured carbide-free bainitic steels. Wear 2020;460–461:203484.
[47] Kalácska Á, De Baets P, Ben Hamouda H, Theuwissen K, Sukumaran J. Tribological investigation of abrasion resistant steels with martensitic and retained austenitic microstructure in single- and multi–asperity contact. Wear 2021:482–3.
[48] Callahan M, Hubert O, Hild F, Perlade A, Schmitt JH. Coincidence of strain-induced TRIP and propagative PLC bands in Medium Mn steels. Mater Sci Eng, A 2017;704:391–400.
[49] Guo H, Zhao A, Zhi C, Ding R, Wang J. Two-body abrasion wear mechanism of super bainitic steel. Mater Sci Technol 2017;33:893–8.
[50] Godefroid LB, Souza AT, Pinto MA. Fracture toughness, fatigue crack resistance and wear resistance of two railroad steels. J Mater Res Technol 2020;9:9588–97.
[51] Xu Y, Fang L, Cen Q, Zhu J. Nano structure and transformation mechanism of white layer for AISI1045 steel during impact wear. Wear 2005;258:537–44.
[52] Zhang F, Duan C, Sun W, Ju K. Effects of cutting conditions on the microstructure and residual stress of white and dark layers in cutting hardened steel. J Mater Process Technol 2019;266:599–611.
[53] Peng SG, Song RB, Sun T, Yang FQ, Deng P, Wu CJ. Surface failure behavior of 70Mn martensite steel under abrasive impact wear. Wear 2016;362–363:129–34.
[54] Han R, Yang G, Zhao G, Sun X, Zhu X. Strengthening mechanism and three-body impact abrasive wear behavior of the hot-rolled air-cooling martensitic wear resistant steel. J Mater Res Technol 2023;24:3023–32.